

Capacity retention behavior and morphology evolution of $\text{Si}_x\text{Ge}_{1-x}$ nanoparticles as lithium-ion battery anode

This content has been downloaded from IOPscience. Please scroll down to see the full text.

2015 Nanotechnology 26 255702

(<http://iopscience.iop.org/0957-4484/26/25/255702>)

View [the table of contents for this issue](#), or go to the [journal homepage](#) for more

Download details:

IP Address: 128.125.124.146

This content was downloaded on 10/09/2015 at 18:39

Please note that [terms and conditions apply](#).

Capacity retention behavior and morphology evolution of $\text{Si}_x\text{Ge}_{1-x}$ nanoparticles as lithium-ion battery anode

Mingyuan Ge^{1,8}, Seongbeom Kim^{2,3,8}, Anmin Nie⁴,
Reza Shahbazian-Yassar⁴, Matthew Mecklenburg⁵, Yunhao Lu⁶, Xin Fang¹,
Chenfei Shen¹, Jiepeng Rong¹, Song Yi Park², Dong Suk Kim⁷,
Jin Young Kim² and Chongwu Zhou¹

¹ Department of Electrical Engineering and Department of Chemical Engineering and Materials Science, University of Southern California, Los Angeles, CA 90089, USA

² School of Energy and Chemical Engineering, Ulsan National Institute of Science and Technology (UNIST), Ulsan 689-798, Korea

³ Department of Chemical and Biological Engineering, University at Buffalo (SUNY), Buffalo, New York 14260-4200, USA

⁴ Department of Mechanical Engineering-Engineering Mechanics, Michigan Technological University, Houghton, Michigan 49931, USA

⁵ Center for Electron Microscopy and Microanalysis, University of Southern California, Los Angeles, CA 90089, USA

⁶ Department of Materials Science and Engineering, Zhejiang University, Hangzhou, Zhejiang, 310027, People's Republic of China

⁷ KIER UNIST Advanced Center for Energy, Korea Institute of Energy Research, Ulsan 689-798, Korea

E-mail: chongwuz@usc.edu and jykim@unist.ac.kr

Received 4 February 2015, revised 24 April 2015

Accepted for publication 29 April 2015

Published 29 May 2015



CrossMark

Abstract

Engineering silicon into nanostructures has been a well-adopted strategy to improve the cyclic performance of silicon as a lithium-ion battery anode. Here, we show that the electrode performance can be further improved by alloying silicon with germanium. We have evaluated the electrode performance of $\text{Si}_x\text{Ge}_{1-x}$ nanoparticles (NPs) with different compositions. Experimentally, $\text{Si}_x\text{Ge}_{1-x}$ NPs with compositions approaching $\text{Si}_{50}\text{Ge}_{50}$ are found to have better cyclic retention than both Si-rich and Ge-rich NPs. During the charge/discharge process, NP merging and Si-Ge homogenization are observed. In addition, a distinct morphology difference is observed after 100 cycles, which is believed to be responsible for the different capacity retention behavior. The present study on $\text{Si}_x\text{Ge}_{1-x}$ alloy NPs sheds light on the development of Si-based electrode materials for stable operation in lithium-ion batteries (e.g., through a comprehensive design of material structure and chemical composition). The investigation of composition-dependent morphology evolution in the delithiated Li-SiGe ternary alloy also significantly broadens our understanding of dealloying in complex systems, and it is complementary to the well-established understanding of dealloying behavior in binary systems (e.g., Au-Ag alloys).

 Online supplementary data available from stacks.iop.org/NANO/26/255702/mmedia

Keywords: SiGe alloy, structure evolution, lithium-ion battery anode

(Some figures may appear in colour only in the online journal)

⁸ Mingyuan Ge and Seongbeom Kim contributed equally to this work.

1. Introduction

Silicon, with its high theoretical capacity (3600 mAh g^{-1}), has emerged as a promising anode candidate for lithium-ion batteries. However, the intrinsic properties of silicon, including its large volume change during the lithiation/delithiation cycles, lead to severe electrode pulverization and capacity loss, and thus have hampered its practical usage [1]. Recently, strategies for engineering silicon into nanostructures have been prevalently adopted, with the goal of providing additional free space to accommodate volume expansion [2–4]. In addition, the structural integrity of silicon during the lithiation step has been intensively investigated both theoretically and experimentally, and these investigations could provide guidance for better structural designs that may lead to further performance improvements. For example, recent achievements include the successful synthesis of a variety of nanostructures such as silicon nanowires [5–7], silicon hollow structures [8–11], and porous silicon [12–16], which have significantly advanced the cyclic performance of the silicon anode. In addition, increased fundamental understanding of its structural evolution has been achieved by taking advantage of *in situ* TEM observation [17–20], which has disclosed the correlation between structural integrity and particle size. For instance, silicon NPs smaller than 150 nm are free to expand without initiating cracks when lithium atoms are inserted [21].

Apart from adapting the structural design of silicon to stabilize its cyclic performance, strategies for modifying its chemical functionality, such as alloying silicon with other elements, also deserve critical research attention. For example, a thin layer of carbon coating on the silicon anode will considerably suppress the decomposition of electrolytes on the silicon surface, and therefore will significantly improve the electrochemical behavior of the silicon anode [22]. Other silicon-carbon composites such as silicon embedded in a variety of carbon matrices also demonstrate improved electrode performance. In these composites, the carbon matrix significantly increased the electrode conductivity and buffered a large volume change of silicon during lithium ion insertion and extraction [23–26]. Apart from the carbon additive, understanding the electrochemical performance of silicon alloyed with other elements is of great interest and importance, since adding additional elements will provide additional degrees of freedom to tune the material properties, which could be beneficial to the development of an advanced silicon-based battery anode with high capacity and long cyclic life. In addition, researching the structural evolution of a delithiated Li-SiX multicomponent system and examining the effect of the added components to the resultant morphology may disclose rich information, because it is much more complicated than—and complementary to—the well-established understanding of dealloying behavior in binary systems (e.g., Au-Ag alloys [27–29]). This dealloying behavior has already generated a significant impact on the fabrication of nanoporous materials for various applications, including catalysis [30, 31], sensing [32], and supercapacitors [33].

The SiGe alloy is one of the most interesting and simple material systems for lithium-ion battery anodes. The simplicity of this prototypical alloy lies in the almost identical lithiation and delithiation behavior of Li-Si and Li-Ge binary systems [34–37], which make the SiGe alloy an ideal choice for identifying the effect of the added components in the dealloying process. Previous research indicates that a better rate capability can be reached in multilayered Si-Ge films than in pure Si [38, 39] due to the high electronic conductivity of Ge [40]. Studies of $\text{Si}_x\text{Ge}_{1-x}$ alloy thin films also demonstrate that the capacity retention of the electrode material can be significantly improved with an increase of the Ge fraction [41]. While significant progress has been made in the study of SiGe films for battery applications, little attention has been given to SiGe NPs, which are of great interest and may display different battery performance than SiGe thin films due to their morphology differences.

Here we evaluate the battery performance of $\text{Si}_x\text{Ge}_{1-x}$ alloy NPs, and we report on the morphology evolution of the NPs at a delithiated state after the 1st, 5th, and 100th cycles. Interestingly, NP merging is found at an early stage of cycling, suggesting the existence of strong collective and synergetic effects among the NPs during the lithiation/delithiation process, which is consistent with a previous report on the merging of pure Si NPs [42] and the welding of silicon nanowires [43]. Furthermore, merged NPs are found to continually evolve into interconnected porous structures after long lithiation/delithiation cycling, which is absent in previous *in situ* TEM studies on silicon NPs [19] and nanowires [43]. In addition, $\text{Si}_x\text{Ge}_{1-x}$ NPs with compositions close to $\text{Si}_{50}\text{Ge}_{50}$ are found to be more stable than pure silicon and other SiGe compositions in repeated cyclic tests, which implies the correlation between composition and morphology evolution during cycling.

2. Results and discussion

High vacuum-based deposition techniques such as molecular beam epitaxy and chemical vapor deposition have been commonly adopted to engineer atomic fractions of silicon and germanium as a thin film onto a substrate. Even though these techniques can finely tune the composition ratio, which is appropriate for electronic applications, they require high temperature processes and high vacuum systems with limited growth rates. While the growth of pristine silicon [44] and germanium NPs [45] using solution-based chemical approaches with high production yield has previously been reported, no research has been published on SiGe alloy NPs using solution methods. In this work, we have chosen to use laser pyrolysis of the gaseous precursor for SiGe alloy NP synthesis [46–48]. A focused laser beam (wavelength $10.6 \mu\text{m}$) was aligned to cross the gas flow line perpendicularly within the reaction chamber. The gas mixtures were jetted from two coaxially aligned tubes; reaction gas mixtures flew through the inner tube and the He gas flew through the outer tube to confine reaction gases and products. All the gas flows were regulated by mass flow controllers. SiH_4 (99.9999%, Daesung

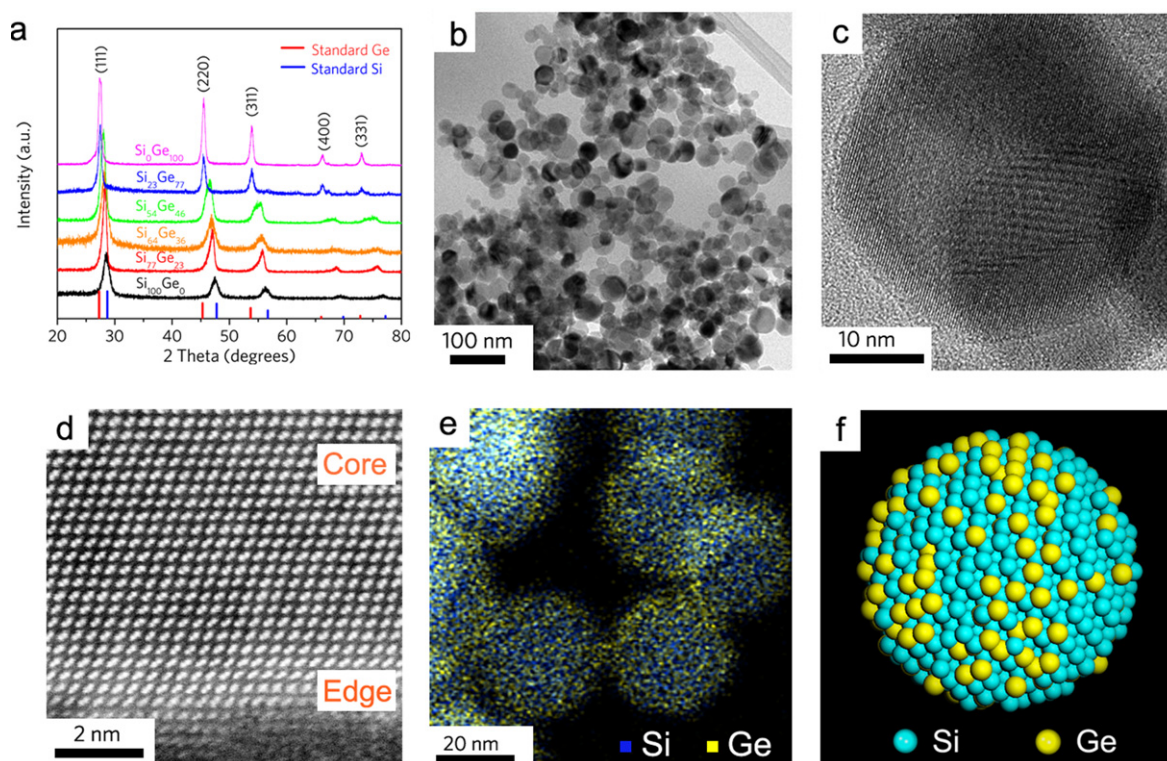


Figure 1. Structural characterization of as-synthesized $\text{Si}_x\text{Ge}_{1-x}$ NPs. (a) XRD of various $\text{Si}_x\text{Ge}_{1-x}$ samples indicate their single phases. (b) TEM and (c) HAADF-STEM images of $\text{Si}_{77}\text{Ge}_{23}$ NPs at different magnifications. The subtle contrast difference in (d) high-resolution HAADF-STEM indicates the nonhomogeneity of Si-Ge distribution at an atomic scale. (e) Elemental distribution of Si (blue) and Ge (yellow) of the $\text{Si}_{77}\text{Ge}_{23}$ sample. (f) A schematic model illustrates the nonhomogeneity of Si-Ge.

Industrial Gases Co., Ltd) and GeH_4 (99.999%, 10% diluted in H_2 , Voltaix Inc.) gases were used as feed stocks for $\text{Si}_x\text{Ge}_{1-x}$ NPs, and SF_6 was used as a photosensitizer gas to promote the dissociation of SiH_4 and GeH_4 . The flow of SiH_4 was fixed to 25 sccm/min, while the flow of GeH_4 was varied to control the composition ratio of Ge within the $\text{Si}_x\text{Ge}_{1-x}$ alloy NPs. The pressure of the reaction chamber was maintained at 400 Torr during the synthesis process. The NPs were collected at a membrane filter installed in a tightly sealed collector and transferred to a glove box without exposure to the air. A typical production yield of SiGe alloy NPs is more than 3 g h^{-1} using a pilot setup with a 60 W maximum power CO_2 laser. The production yield is primarily limited by the power of the laser beam, which is implicative of possible scale-up considering the multi-kW CO_2 lasers that are currently commercially available. Contact-free synthesis and continuous process are the outstanding features of the laser pyrolysis technique, which is taken into account in this study.

As-synthesized $\text{Si}_x\text{Ge}_{1-x}$ (x in the range from 0 to 1.0) NPs were characterized to be in single phase in the x-ray diffraction (XRD) pattern (figure 1(a)), and the peak shifts among different samples illustrate the composition difference, which was further confirmed through energy dispersive x-ray analysis (EDX) performed with a transmission electron microscope (TEM). The atomic concentration in these NPs was determined to be $\text{Si}_{100}\text{Ge}_0$, $\text{Si}_{77}\text{Ge}_{23}$, $\text{Si}_{64}\text{Ge}_{36}$, $\text{Si}_{54}\text{Ge}_{46}$, $\text{Si}_{23}\text{Ge}_{77}$, and $\text{Si}_0\text{Ge}_{100}$, respectively, which correlates with

the molar ratio of the SiH_4 -to- GeH_4 gas precursor, as shown in figure S1 in the Supporting Information. The structures of all samples with different $\text{Si}_x\text{Ge}_{1-x}$ compositions are quite similar. The average size of the NPs was determined to be less than 30 nm, with small differences for all compositions based on a statistic analysis, using TEM, over 40 NPs for each sample. The small size of the NPs is also revealed by the broadening of diffraction peaks and their subtle differences in the full width at half maximum in XRD. A large view of NP morphology shown in the SEM images (supporting information, figure S2) confirms the uniformity of NP size and the nonexistence of very large NPs (e.g., larger than 100 nm), suggesting that NPs can maintain integrity during the charge/discharge process, and thus it is safe to preclude the NP size effect to electrode performance.

Here we take the $\text{Si}_{77}\text{Ge}_{23}$ sample as an example, and we present its typical results. TEM images in figures 1(b) and (c) show the NP's morphology at different magnifications. The NPs are spherical, with a relatively uniform size of approximately 25 nm in diameter. A highly crystallized structure is revealed by the lattice fringe shown both in figure 1(c) and in the atomic resolution image shown in the high-angle annular dark field scanning TEM (HAADF-STEM) image in figure 1(d). It is interesting to note the existence of a subtle contrast difference of the atoms in the HAADF image in figure 1(d). For example, the bright region at the outer surface indicates the Ge enrichment, which was further characterized

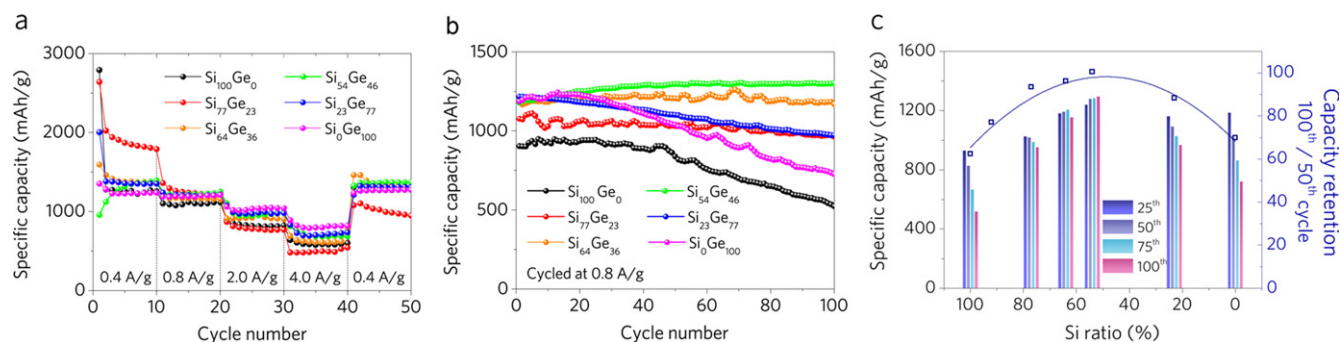


Figure 2. Electrochemical performance of $\text{Si}_x\text{Ge}_{1-x}$ NPs as lithium-ion battery anode. (a) Capacity of the cells at different current rates. (b) Continued cyclic tests up to 100 cycles, which show a dramatic difference in terms of capacity retention. (c) Capacities at the 25th, 75th, and 100th cycles of $\text{Si}_x\text{Ge}_{1-x}$ were compared at a current rate of 0.8 A g^{-1} . The capacity retention of $\text{Si}_x\text{Ge}_{1-x}$ NPs, defined as the ratio of capacity at the 100th cycle with respect to the capacity at the 50th cycle, is shown as the square symbol in the figure 2(c).

and clearly visualized in the Si-Ge elemental distribution map based on the EDX image shown in figure 1(e), since enriched Ge can be found at the periphery of the NPs. The Ge enrichment (or segregation) at the NP surface will lower the surface energy to stabilize the SiGe nanostructure, which has been demonstrated in the epitaxially grown SiGe alloy [49]. Figure 1(f) presents a schematic atomic model of the SiGe NP. In the Raman scattering spectra, the coexistence of Raman shifts of Si-Si, Si-Ge, and Ge-Ge vibrations also indicate the nonhomogeneous features of the alloy sample at the atomic scale (supporting information, figure S3).

Coin cells were made to evaluate the electrochemical properties of the SiGe NPs. Specifically, NPs were mixed with carbon black and sodium alginate (as a binder) with a mass ratio of 7:2:1 to form a slurry, which was further coated on top of copper foils with a doctor's blade and dried to get the electrode.

Figure 2(a) shows the specific capacity of cells with different compositions at different current rates. Except for the capacity difference in the first several cycles, the following cycles show stable and qualitatively similar capacity retention behavior at various current rates. However, continued cyclic tests up to 100 cycles show a dramatic difference in terms of capacity retention, as presented in figure 2(b). Figure 2(c) summarizes the electrode capacities for each $\text{Si}_x\text{Ge}_{1-x}$ composition at different cyclic states. If we define the capacity retention as the percentage of the capacity at the 100th cycle with respect to the capacity at the 50th cycle, it is found that the $\text{Si}_x\text{Ge}_{1-x}$ alloy NPs with composition ratios around 1:1 ($\text{Si}_{54}\text{Ge}_{46}$ sample) have higher capacity retention than both Si-rich and Ge-rich alloy NPs.

To reveal the difference, batteries were disassembled and the NP's morphology was checked to shed light on the observed difference in capacity retention for the $\text{Si}_{77}\text{Ge}_{23}$, $\text{Si}_{54}\text{Ge}_{46}$, and $\text{Si}_{23}\text{Ge}_{77}$ samples. Figure 3 shows the morphology of the delithiated SiGe sample ($\text{Si}_{77}\text{Ge}_{23}$, $\text{Si}_{54}\text{Ge}_{46}$, and $\text{Si}_{23}\text{Ge}_{77}$) after the first and fifth cycles. Note that the individual NPs are merged together and form large structures after the first lithiation/delithiation cycle for all three samples

(figures 3(a)–(c)), indicating a strong interparticle interaction (e.g., atomic diffusion between neighboring NPs). The phenomenon of NP merging is absent in previous reports on the *in situ* TEM study of isolated Si NPs or nanowires [18, 50], suggesting the complicated collective behavior of electrode materials in a confined environment (e.g., NPs compacted in a battery case) compared to those in an interaction-free environment. Figures 3(d)–(f) present the structure of delithiated NPs after 5 cycles, and no significant morphology change is observed.

After 100 cycles, all three samples have porous structures, as indicated in figure 4. It is noticeable that the Si-rich sample ($\text{Si}_{77}\text{Ge}_{23}$, figures 4(a)–(d)) and the Ge-rich sample ($\text{Si}_{23}\text{Ge}_{77}$, figures 2(i)–(l)) are fluffy, show a similar morphology with larger ligaments, and enclose larger void holes than the $\text{Si}_{54}\text{Ge}_{46}$ sample (figures 4(e)–(h), with TEM images found in the supporting information). It is reasonable to relate the different capacity retention behavior to the structural differences in the various $\text{Si}_x\text{Ge}_{1-x}$ compositions. We suggest that the structural evolution from the merged NPs to the resultant fluffy structure of the Si-rich and Ge-rich samples exposes more surface area to the electrolytes than the $\text{Si}_{54}\text{Ge}_{46}$ sample, resulting in the formation of a larger portion of the solid electrolyte interface and leading to successive capacity degradation, as indicated in figure 2.

The composition-dependent morphology evolution in the delithiated Li-SiGe system is unexpected considering the similarity of the chemical properties of Si and Ge. To uncover the underlying physical mechanism, it is interesting to ask two questions: 1. For certain $\text{Si}_x\text{Ge}_{1-x}$ compositions, how does the Si-Ge atomic distribution change during the structural evolution? 2. What is the driving force for the structural evolution, and why are NPs merged after cycling? figures 4(d), (h), and (i) illustrate the elemental distribution of Si and Ge after the 100th cycle. It is found that Si and Ge are uniformly distributed in the amorphous porous structures in all three samples, which is different from the initial state, which features nonhomogeneous Si-Ge distribution. The Si-Ge homogenization under the dealloying process of Li-SiGe

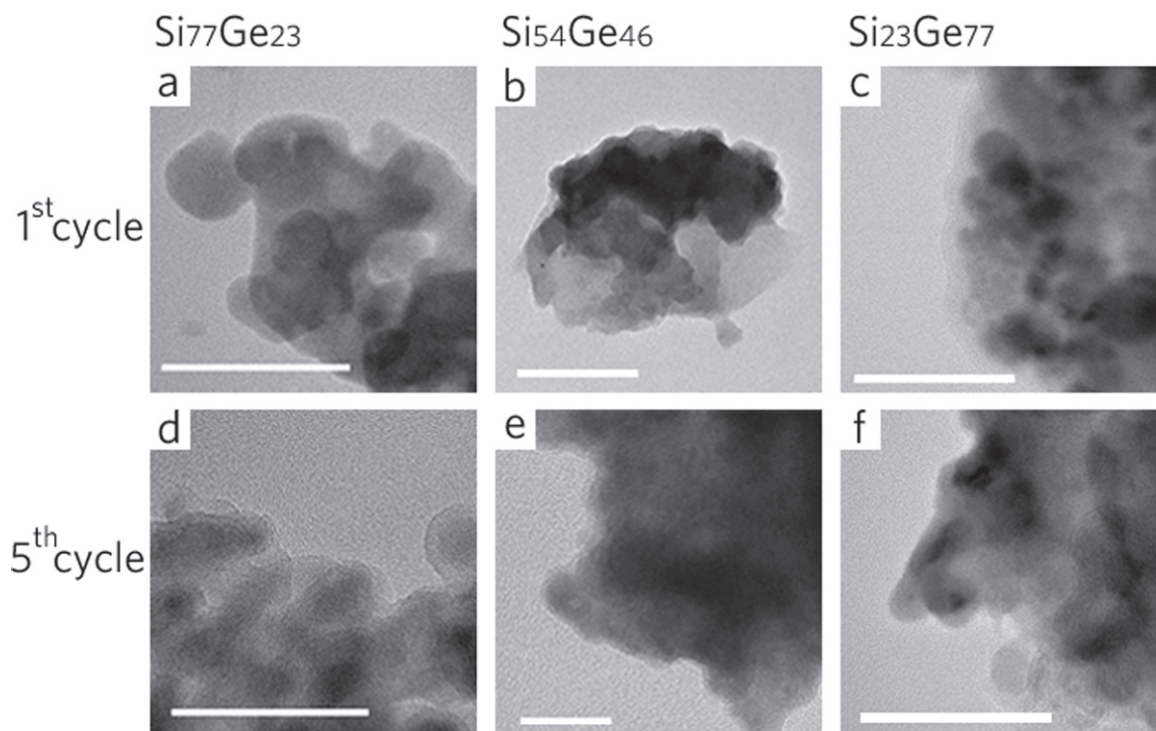


Figure 3. Morphology of delithiated (dealloyed) $\text{Si}_x\text{Ge}_{1-x}$ after the 1st and 5th lithiation/delithiation cycles. TEM images of (a)–(d), (b)–(e), and (c)–(f) show the morphology of $\text{Si}_{77}\text{Ge}_{23}$, $\text{Si}_{54}\text{Ge}_{46}$, and $\text{Si}_{23}\text{Ge}_{77}$ after the 1st and 5th cycle, respectively. It is clear the particles for all three samples are merged together. Scale bar is 100 nm for all images.

appears as a generic phenomenon in the Si-Ge compositions we studied. Because the diffusion rates of Si and Ge are extremely low at room temperature [51], interdiffusion between Si and Ge is therefore inferred to have minimal effect on the homogenization. From an *ab initio* molecular dynamic simulation illustrated below, extraction of Li from the SiGe host is found to dramatically accelerate the mixing of Si and Ge.

The structure of the $\text{Li}_{15}(\text{Si}_{0.5}\text{Ge}_{0.5})_4$ crystal shown in figure 5(a) was constructed to simulate the lithiated Li-SiGe alloy; a nonuniform Si and Ge distribution was created to simulate the nonhomogeneity. *Ab initio* molecular dynamic (MD) simulations were performed using the *Vienna Ab-initio Simulation Package* code [52], and ultrasoft pseudopotentials were used to model electron-ion interactions. Structure relaxation was carried out using the generalized gradient approximation for the exchange-correlation function [53]. The k-space integration was completed by summing over the Monkhorst-Pack special points in the Brillouin zone. The Gaussian method with a smearing width of 0.05 eV was used to determine the Fermi level. The plane wave basis set was restricted by a cutoff energy of 425 eV. A periodic nanocube containing $\text{Li}_{480}\text{Si}_{64}\text{Ge}_{64}$ atoms was constructed with a vacant layer of 15 nm in three dimensions to eliminate the interference from the neighboring mirror structure. $1 \times 1 \times 1$ k-point mesh was used for energy calculations. To simulate the delithiation (dealloying) process of Li-SiGe, Li atoms were removed from the outermost layers after every 50 fs MD simulation. The Si-

Ge radial distribution function was calculated during the MD simulation. Note that this simulated structure (2 nm in dimension) is smaller than the NPs used in this study in order to make simulation tractable. The pair distribution function (PDF) of Si-Ge was calculated to evaluate the intermixing of Si and Ge (figure 5(b)). As shown in the PDF, the nearest atom-to-atom distance of Si and Ge is around 5 Å at the early stage of the simulation (0–150 fs), corresponding to the distance of Si and Ge in the lithiated $\text{Li}_{15}(\text{Si}_x\text{Ge}_{1-x})_4$ structure. As the delithiation process proceeds, when the frontier of delithiation comes across the Si-Ge interface, a small peak equivalent to a bond length of 2.5 Å starts to show up (e.g. 250 fs), which is inferred as the normal bonding length in the SiGe alloy. The intensity of the peak continues to increase, evincing an intensification of Si-Ge interdiffusion to form a homogeneous alloy. The images in figure 5(c) display the particle structure at successive simulation stages, showing the mixing of Si-Ge during the delithiation process, which eventually results in an amorphous particle. The observed fast atom relocation is striking considering the low atomic diffusion rate of Si and Ge. However, with the aid of delithiation, extraction of Li leaves a large space between the Si and/or Ge. The instability of Si and/or Ge atoms staying far away from each other induces a large diffusion rate. Based on the fast atomic diffusion observed in simulation, it is reasonable to infer that when particles contact each other, interparticle diffusion is plausible and will initiate particle merging, as shown in figure 3 in the experiments.

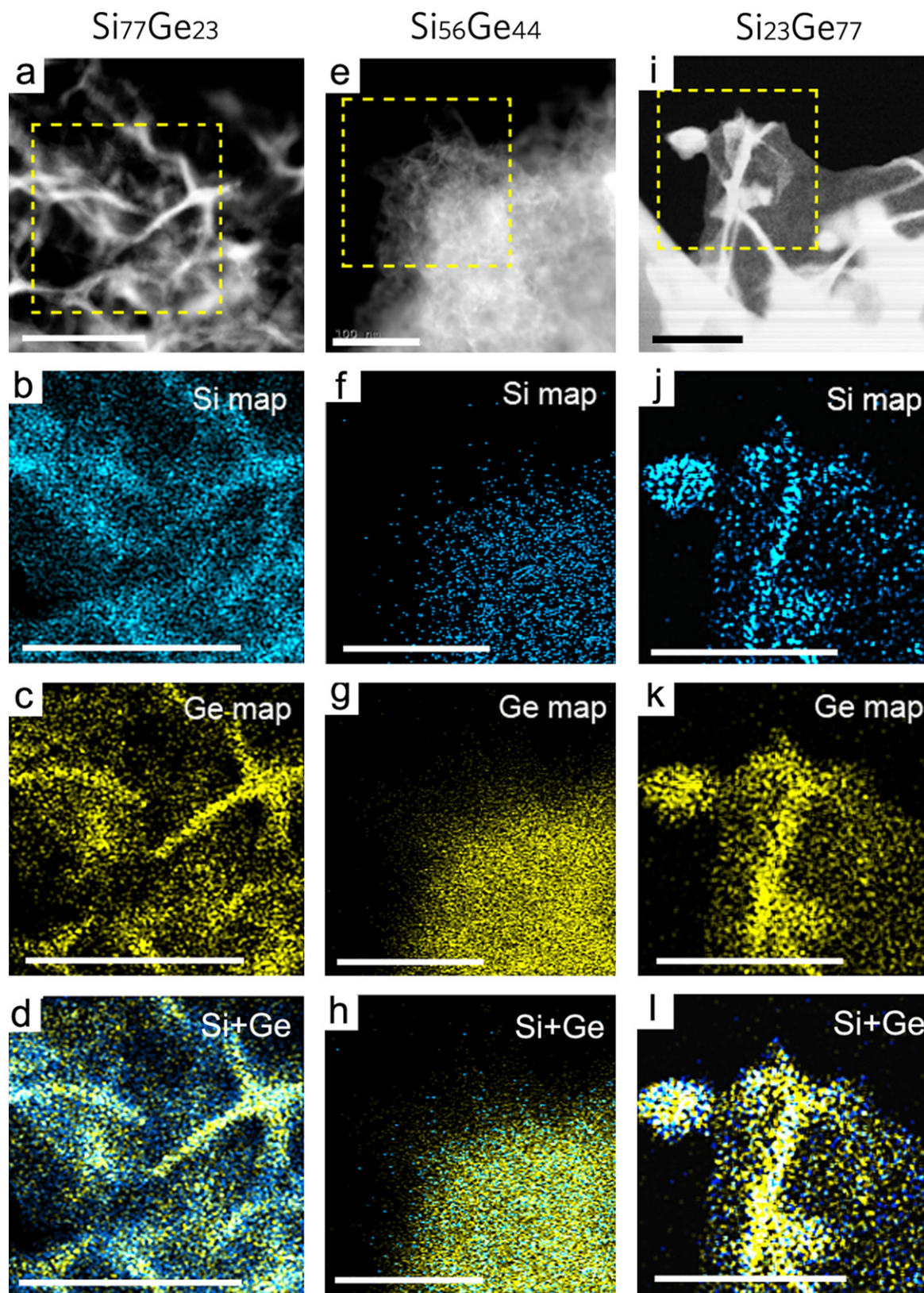


Figure 4. Morphology of delithiated (dealloyed) $\text{Si}_x\text{Ge}_{1-x}$ after the 100th lithiation/delithiation cycle. After the 100th cycle, particles evolve into loose structures, as shown in the STEM images in (a), (e), and (i). (a) $\text{Si}_{77}\text{Ge}_{23}$ and (i) $\text{Si}_{23}\text{Ge}_{77}$ are found enclosing larger pores compared to (e) $\text{Si}_{54}\text{Ge}_{46}$. EDX mapping is performed within the dashed square regions in STEM. EDX of (b), (f), (j) Si and (c), (g), (k) Ge, and (d), (h), (l) a combination of Si and Ge demonstrate that Si and Ge have almost homogeneous distribution after the 100th cycles. Scale bar is 100 nm for all images.

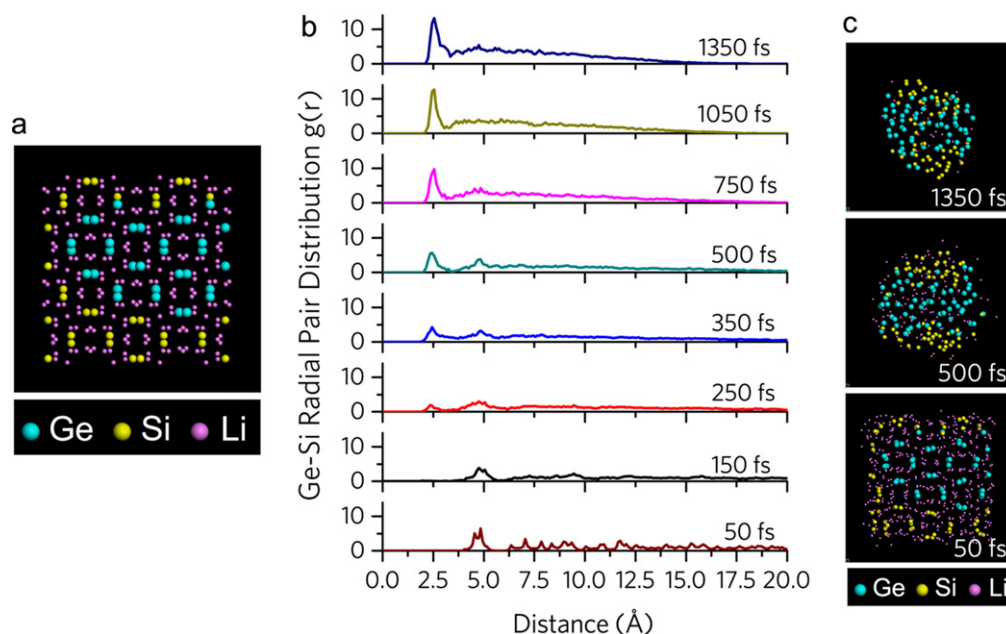


Figure 5. Simulated delithiation process of Li-SiGe and calculated energy diagram of $\text{Si}_x\text{Ge}_{1-x}$. (a) A modeled structure of $\text{Li}_{15}(\text{Si}_{0.5}\text{Ge}_{0.5})_4$ to simulate the lithiated Li-SiGe alloy; a nonuniform Si and Ge distribution was created to simulate the nonhomogeneity. (b) Ge-Si PDF at different stages of the simulated delithiation process. The appearance and increasing intensity of the peak at 2.5 Å indicate the intermixing of Si and Ge to form a homogenized alloy. (c) Atomic structure and morphology of the particle at different simulation states.

In addition, the mixing entropy that characterizes the thermodynamic disorder of the materials will increase during the intermixing of Si-Ge with the incorporation of Ge, and this is responsible for structural stability. In the case of $\text{Si}_x\text{Ge}_{1-x}$, entropy can be calculated as $S = -R[x\ln x + (1-x)\ln(1-x)]$, where $R = 8.314 \text{ J mol}^{-1}\text{K}^{-1}$ is the gas constant. The entropy reaches its maximum at the composition of $x=0.5$ and reaches its minimum at $x=0$ and $x=1.0$. We believe the large entropy of the Si-Ge balanced composition helps stabilize the structure against repeated cycling. We suggest that the improved stability of the porous structure formed in $\text{Si}_{54}\text{Ge}_{46}$ NPs after several reaction cycles may be responsible for its good capacity retention. However, other SiGe compositional NPs are continually both evolving into even more highly porous structures and exposing new electrode-electrolyte interfaces, eventually consuming the active electrode material. Our findings, meanwhile, could be interpreted in a different way from similar SiGe systems [41], which report that the capacity retention improves with an increase of the Ge fraction. However, we suggest that the morphology of the material (NP versus thin film) also could influence the electrochemical behavior of the anode materials.

3. Conclusions

We have successfully synthesized SiGe NPs with adjustable compositions. We found that $\text{Si}_x\text{Ge}_{1-x}$ NPs close to the $\text{Si}_{50}\text{Ge}_{50}$ composition have better cyclic performance (better capacity retention) than both Si-rich and Ge-rich NPs as anode materials for lithium-ion batteries, which is supported

by their morphology difference as observed through TEM after 100 cycles. In addition, two interesting features are disclosed for the first time. NP merging and Si-Ge homogenization are observed during repeated charge/discharge cycles, which are related to the fast atomic rearrangement of Si-Ge with the aid of lithium atom removal, as elucidated in both MD simulation and experiments. We note that conventionally, congregation of the particles during cycling will lower the surface-to-volume ratio, and thus diminish the specific capacity. However, in the case of the SiGe NPs we studied in this work, continuous structural evolution into porous networks leads to large surface area, which will facilitate the Li^+ ion transfer from electrolyte to active material. More importantly, a stable porous structure in an Si-Ge balanced composition helps it maintain its structural integrity without being pulverized and losing capacity. We believe our results will not only shed light on the research on stable Si-based anode materials, but also initiate research on dealloying behavior in complex systems, such as the delithiation process in ternary Li-SiGe compounds beyond binary alloys.

Acknowledgments

Professor Chongwu Zhou's group would like to acknowledge the collaboration of this research with King Abdul-Aziz City for Science and Technology (KACST) via The Center of Excellence for Green Nanotechnologies (CEGN). Some of the images and data used in this article were generated at The Center for Electron Microscopy and Microanalysis, University of Southern California. The synthesis of SiGe

nanoparticles is partially supported by Development Program of the Korean Institute of Energy Research (KIER) (B4-2424).

References

- [1] Boukamp B A, Lesh G C and Huggins R A 1981 All-solid lithium electrodes with mixed-conductor matrix *J. Electrochem. Soc.* **128** 725–9
- [2] Szczech J R and Jin S 2011 Nanostructured silicon for high capacity lithium battery anodes *Energy Environ. Sci.* **4** 56–72
- [3] Wu H and Cui Y 2012 Designing nanostructured Si anodes for high energy lithium ion batteries *Nano Today* **7** 414–29
- [4] Graetz J, Ahn C C, Yazami R and Fultz B 2003 Highly reversible lithium storage in nanostructured silicon *Electrochem. Solid State* **6** A194–7
- [5] Chan C K et al 2008 High-performance lithium battery anodes using silicon nanowires *Nat. Nanotechnology* **3** 31–5
- [6] Ruffo R, Hong S S, Chan C K, Huggins R A and Cui Y 2009 Impedance analysis of silicon nanowire lithium ion battery anodes *J. Phys. Chem. C* **113** 11390–8
- [7] Peng K Q, Jie J S, Zhang W J and Lee S T 2008 Silicon nanowires for rechargeable lithium-ion battery anodes *Appl. Phys. Lett.* **93** 033105
- [8] Yao Y et al 2011 Interconnected silicon hollow nanospheres for lithium-ion battery anodes with long cycle life *Nano Lett.* **11** 2949–54
- [9] Huang X K et al 2014 Controllable synthesis of hollow Si anode for long-cycle-life lithium-ion batteries *Adv. Mater.* **26** 4326–32
- [10] Park M H et al 2009 Silicon nanotube battery anodes *Nano Lett.* **9** 3844–7
- [11] Wu H et al 2012 Stable cycling of double-walled silicon nanotube battery anodes through solid-electrolyte interphase control *Nat. Nanotechnology* **7** 309–14
- [12] Ge M, Fang X, Rong J and Zhou C 2013 Review of porous silicon preparation and its application for lithium-ion battery anodes *Nanotechnology* **24** 422001
- [13] Ge M Y, Rong J P, Fang X and Zhou C W 2012 Porous doped silicon nanowires for lithium ion battery anode with long cycle life *Nano Lett.* **12** 2318–23
- [14] Ge M Y et al 2013 Scalable preparation of porous silicon nanoparticles and their application for lithium-ion battery anodes *Nano Res.* **6** 174–81
- [15] Ge M Y et al 2014 Large-scale fabrication, 3D tomography, and lithium-ion battery application of porous silicon *Nano Lett.* **14** 261–8
- [16] Zhao Y, Liu X Z, Li H Q, Zhai T Y and Zhou H S 2012 Hierarchical micro/nano porous silicon Li-ion battery anodes *Chem. Commun.* **48** 5079–81
- [17] Liu X H et al 2011 Anisotropic swelling and fracture of silicon nanowires during lithiation *Nano Lett.* **11** 3312–8
- [18] McDowell M T et al 2013 *In situ* TEM of two-phase lithiation of amorphous silicon nanospheres *Nano Lett.* **13** 758–64
- [19] Gu M et al 2012 *In situ* TEM study of lithiation behavior of silicon nanoparticles attached to and embedded in a carbon matrix *ACS Nano* **6** 8439–47
- [20] McDowell M T et al 2012 Studying the kinetics of crystalline silicon nanoparticle lithiation with *in situ* transmission microscopy *Adv. Mater.* **24** 6034–41
- [21] Liu X H et al 2012 Size-dependent fracture of silicon nanoparticles during lithiation *ACS Nano* **6** 1522–31
- [22] Yoshio M et al 2002 Carbon-coated Si as a lithium-ion battery anode material *J. Electrochem. Soc.* **149** A1598–603
- [23] Ng S H et al 2006 Highly reversible lithium storage in spheroidal carbon-coated silicon nanocomposites as anodes for lithium-ion batteries *Angew. Chem. Int. Ed. Engl.* **45** 6896–9
- [24] Huang R, Fan X, Shen W C and Zhu J 2009 Carbon-coated silicon nanowire array films for high-performance lithium-ion battery anodes *Appl. Phys. Lett.* **95** 133119
- [25] Cui L F, Yang Y, Hsu C M and Cui Y 2009 Carbon-silicon core-shell nanowires as high capacity electrode for lithium ion batteries *Nano Lett.* **9** 3370–4
- [26] Cui L F, Hu L B, Choi J W and Cui Y 2010 Light-weight free-standing carbon nanotube-silicon films for anodes of lithium ion batteries *ACS Nano* **4** 3671–8
- [27] Jia F L, Yu C F, Deng K J and Zhang L Z 2007 Nanoporous metal (Cu, Ag, Au) films with high surface area: General fabrication and preliminary electrochemical performance *J. Phys. Chem. C* **111** 8424–31
- [28] Erlebacher J, Aziz M J, Karma A, Dimitrov N and Sieradzki K 2001 Evolution of nanoporosity in dealloying *Nature* **410** 450–3
- [29] Chen Q and Sieradzki K 2013 Spontaneous evolution of bicontinuous nanostructures in dealloyed Li-based systems *Nat. Mater.* **12** 1102–6
- [30] Ding Y, Chen M W and Erlebacher J 2004 Metallic mesoporous nanocomposites for electrocatalysis *J. Am. Chem. Soc.* **126** 6876–7
- [31] Xu C X et al 2007 Low temperature CO oxidation over unsupported nanoporous gold *J. Am. Chem. Soc.* **129** 42–3
- [32] You T Y, Niwa O, Tomita M and Hirono S 2003 Characterization of platinum nanoparticle-embedded carbon film electrode and its detection of hydrogen peroxide *Anal. Chem.* **75** 2080–5
- [33] Lang X Y, Hirata A, Fujita T and Chen M W 2011 Nanoporous metal/oxide hybrid electrodes for electrochemical supercapacitors *Nat. Nanotechnology* **6** 232–6
- [34] Choi J W et al 2010 Stepwise nanopore evolution in one-dimensional nanostructures *Nano Lett.* **10** 1409–13
- [35] Obrovac M N and Christensen L 2004 Structural changes in silicon anodes during lithium insertion/extraction *Electrochem. Solid State* **7** A93–6
- [36] Laforge B, Levan-Jodin L, Salot R and Billard A 2008 Study of germanium as electrode in thin-film battery *J. Electrochem. Soc.* **155** A181–8
- [37] Liu X H et al 2011 Reversible nanopore formation in Ge nanowires during lithiation-delithiation cycling: an *in situ* transmission electron microscopy study *Nano Lett.* **11** 3991–7
- [38] Song T et al 2012 Si/Ge double-layered nanotube array as a lithium ion battery anode *ACS Nano* **6** 303–9
- [39] Hwang C M, Lim C H and Park J W 2011 Evaluation of Si/Ge multi-layered negative film electrodes using magnetron sputtering for rechargeable lithium ion batteries *Thin Solid Films* **519** 2332–8
- [40] Conwell E M 1952 Properties of silicon and germanium *P. Ire.* **40** 1327–37
- [41] Abel P R et al 2013 Nanostructured Si(i-x)Ge_x for tunable thin film lithium-ion battery anodes *ACS Nano* **7** 2249–57
- [42] Li H et al 2000 The crystal structural evolution of nano-Si anode caused by lithium insertion and extraction at room temperature *Solid State Ion.* **135** 181–91
- [43] Karki K et al 2012 Lithium-assisted electrochemical welding in silicon nanowire battery electrodes *Nano Lett.* **12** 1392–7
- [44] Baldwin R K et al 2002 Room temperature solution synthesis of alkyl-capped tetrahedral shaped silicon nanocrystals *J. Am. Chem. Soc.* **124** 1150–1
- [45] Lu X M, Ziegler K J, Ghezalbash A, Johnston K P and Korgel B A 2004 Synthesis of germanium nanocrystals in high temperature supercritical fluid solvents *Nano Lett.* **4** 969–74

- [46] Erogbogbo F *et al* 2011 Creating ligand-free silicon germanium alloy nanocrystal inks *ACS Nano* **5** 7950–9
- [47] Kim S *et al* 2014 High-yield synthesis of single-crystal silicon nanoparticles as anode materials of lithium ion batteries via photosensitizer-assisted laser pyrolysis *J. Mater. Chem. A* **2** 18070–5
- [48] Kim S *et al* 2014 Size tailoring of aqueous germanium nanoparticle dispersions *Nanoscale* **6** 10156–60
- [49] Kelires P C and Tersoff J 1989 Equilibrium alloy properties by direct simulation—oscillatory segregation at the Si-Ge(100) 2×1 surface *Phys. Rev. Lett.* **63** 1164–7
- [50] Lee S W, McDowell M T, Choi J W and Cui Y 2011 Anomalous shape changes of silicon nanopillars by electrochemical lithiation *Nano Lett.* **11** 3034–9
- [51] Silvestri H H, Bracht H, Hansen J L, Larsen A N and Haller E E 2006 Diffusion of silicon in crystalline germanium *Semicond. Sci. Tech.* **21** 758–62
- [52] Kresse G and Furthmüller J 1996 Efficient iterative schemes for *ab initio* total-energy calculations using a plane-wave basis set *Phys. Rev. B* **54** 11169–86
- [53] Perdew J P *et al* 1992 Atoms, molecules, solids, and surfaces—applications of the generalized gradient approximation for exchange and correlation *Phys. Rev. B* **46** 6671–87